

Band gap tailoring, structural and morphological properties of $\text{Zn}_{0.98-x}\text{Mn}_{0.02}\text{Cu}_x\text{O}$ ($0 \leq x \leq 0.05$) nanopowders by sol–gel method

D. Anbuselvan · S. Muthukumaran

Received: 6 April 2013 / Accepted: 26 June 2013 / Published online: 9 July 2013
© Springer Science+Business Media New York 2013

Abstract $\text{Zn}_{0.98-x}\text{Mn}_{0.02}\text{Cu}_x\text{O}$ ($0 \leq x \leq 0.05$) nanopowders have been synthesized by sol–gel method. The synthesized nanopowders were characterized by powder X-ray diffraction, energy dispersive X-ray spectra, UV–visible spectrophotometer and Fourier transform infrared spectroscopy. The XRD measurement revealed that the prepared nanopowders have different microstructure without changing a hexagonal wurtzite structure. The calculated average crystallite size was decreased from 22.4 to 16.7 nm for $\text{Cu} = 0$ –0.02 then gradually increased to 21.5 nm for $\text{Cu} = 0.05$ which were confirmed by SEM. The change in lattice parameters, shift in X-ray diffraction peaks and the change in energy gap revealed the substitution of Cu^{2+} ions into Zn–Mn–O lattice. The observed red shift of optical energy gap ($E_g \approx 0.27$ eV) at lower concentrations ($\text{Cu} \leq 2\%$) is explained by increasing charge carriers and Moss–Burstein effect meanwhile blue shift ($E_g \approx 0.56$ eV) at higher Cu concentrations ($\text{Cu} > 2\%$) is explained in terms of the distortion of host lattice and generation of defects. The variation of crystallite size was discussed in terms of micro-strain.

1 Introduction

Diluted magnetic semiconductors (DMSs) become one of the ideal candidate materials for spintronics due to the possibility of integration into the existing microelectronic devices [1–4]. Particularly, ZnO based DMSs have considerable attraction due to its large band gap, high refractive

index and large exciton binding energy [5, 6]. It has very attractive research effort due to its unique properties and versatile applications in transparent electronics, hi-tech applications, ultraviolet (UV) light emitters, photo-detectors, surface acoustical wave devices, piezoelectric devices, transparent conducting electrodes and chemical sensors [7–11]. Doping ZnO with magnetic ions such as Cu, Mn induces magnetic properties due to their possible applications in the field of spintronics [12]. Among these different metallic doping elements, Mn and Cu are important because, (i) they are prominent luminescence activator, which can modify the luminescence of ZnO crystals by creating localized impurity levels [13], (ii) they have many physical and chemical properties similar to those of Zn. (iii) they can change microstructure and optical properties of ZnO system [14].

Several physical and chemical methods have been developed to obtain these starting nanocrystals: the solid state reaction [15], chemical vapour transport [16], mechano-chemical processing [17], vapour phase oxidation of Zn powders [18], hydro thermal process [19], sol–gel process [20] and forced hydrolysis in polyol medium [21–25]. Among the different methods, sol–gel is one of the most important methods to prepare the nanopowder. Sol–gel method is a simple and easily reproducible method [26–30]; provide a control over materials composition at molecular level and applicable to large industrial scale fabrication of products at low cost.

The reduced particle size and lattice constants have been described by Arshad et al. [26] with the increase of Cu concentration in the ZnO nanoparticles. Liu et al. [31] observed the room temperature ferromagnetism in $\text{Zn}_{0.97}\text{Cu}_{0.03}\text{O}$ using vibrational sample magnetometer. The influence of shape and hydrogenation on ferromagnetic properties of $\text{Zn}_{0.93}\text{Mn}_{0.04}\text{Cu}_{0.03}\text{O}$ nanoparticles at room temperature was demonstrated by Xu et al. [32]. Han et al. [33] reported in experiments that

D. Anbuselvan · S. Muthukumaran (✉)
PG and Research Department of Physics, H. H. The Rajah's
College (Autonomous), Pudukkottai 622 001, Tamilnadu, India
e-mail: drsmk123@yahoo.co.in

the Curie temperature of the bulk $\text{Zn}_{0.94}\text{Mn}_{0.05}\text{Cu}_{0.01}\text{O}$ samples was above room temperature and the maximum saturation magnetization (M_s) of the sample doped with 1 % Cu became 30 times larger than that of the sample without Cu at room temperature. Shim et al. [34] also prepared the Cu, Mn co-doped ZnO samples with ferromagnetic property at room temperature, but the results showed that the ferromagnetism originated from the secondary phase of $\text{Zn Mn}_2\text{O}_4$. The reduced saturation magnetization was observed by Liu et al. [35] in the Cu doped $\text{Zn}_{0.96}\text{Mn}_{0.04}\text{O}$ system.

Even though some of the research works have been carried out on Cu and Mn co-doped ZnO system [33–35], comprehensive study of the structural, morphological and optical properties of Cu and Mn co-doped ZnO nanopowders is still scanty. Therefore, in the present investigation, Cu, Mn co-doped ZnO ($\text{Zn}_{0.98-x}\text{Mn}_{0.02}\text{Cu}_x\text{O}$, $0 \leq x \leq 0.05$) nanopowders have been synthesized by sol–gel method. The effect of Cu substitution on its structural, optical and morphological properties has been studied extensively. Further, the size dependent properties of the nanoparticles are correlated with band gap.

2 Experimental details

2.1 Preparation of $\text{Zn}_{0.98-x}\text{Mn}_{0.02}\text{Cu}_x\text{O}$, $0 \leq x \leq 0.05$ nanopowders

In the present investigation, $\text{Zn}_{0.98-x}\text{Mn}_{0.02}\text{Cu}_x\text{O}$ ($0 \leq x \leq 0.05$) nanopowders have been synthesized using sol–gel method by the following procedure: The high purity chemicals (>99 % purity) such as Zinc acetate dihydrate ($\text{Zn}(\text{CH}_3\text{CO}_2)_2 \cdot 2\text{H}_2\text{O}$), copper(II) acetate monohydrate ($\text{Cu}(\text{CH}_3\text{CO}_2)_2 \cdot \text{H}_2\text{O}$), manganese(III) acetate tetrahydrate ($\text{Mn}(\text{CH}_3\text{CO}_2)_3 \cdot 4\text{H}_2\text{O}$), *N* dimethyl-formamide (DMF) are used as the precursors for the sample preparation. Initially, appropriate amounts of zinc and manganese acetates were dissolved in DMF and kept in magnetic stirrer for $\frac{1}{2}$ h under constant stirring. Again, the appropriate amount of copper acetate was added into the solution and stirred for another $\frac{1}{2}$ h to prepare the homogeneous and clear solution. The homogeneous solution was stirred at 60 °C for 1 h. Then, the resulting sols were evaporated in hot air furnace and dried by micro-oven for 2 h. The dried gels were collected and grounded in an agate mortar. The same procedure was repeated for other samples preparation. Finally, the collected nanopowders were annealed at 500 °C under air atmosphere for 4 h followed by furnace cooling.

2.2 Characterization techniques

The crystal structure of $\text{Zn}_{0.98-x}\text{Mn}_{0.02}\text{Cu}_x\text{O}$ ($0 \leq x \leq 0.05$) nanopowders was determined by powder X-ray diffraction.

XRD patterns were recorded on a Rigaku C/max-2500 diffractometer using $\text{Cu K}\alpha$ radiation ($\lambda = 1.5408 \text{ \AA}$) operated at 40 kV and 30 mA in the wide angle region from 10° to 80°. The surface morphology of the samples was studied using a scanning electron microscope (SEM, Philip XL 30). The topological features and the composition of Zn, O, Mn and Cu were determined by energy dispersive X-ray spectrometer on K and L lines.

The UV–visible optical absorption and transmittance spectra of Mn-doped and Mn, Cu co-doped ZnO nanopowders have been carried out with a view to explore their optical properties. The spectral absorption spectra were recorded using UV visible spectrophotometer (Model: Lambda 35, Make: Perkin Elmer) in the wavelength ranges from 310 to 1,100 nm using cm^{-1} quartz cuvettes at room temperature. Halogen and deuterium lamp are used as sources for visible and UV radiations, respectively at room temperature.

3 Results and discussion

3.1 X-ray diffraction (XRD)—structural studies

The typical XRD diffraction spectra of $\text{Zn}_{0.98-x}\text{Mn}_{0.02}\text{Cu}_x\text{O}$ ($0 \leq x \leq 0.05$) nanopowders are shown in Fig. 1. The diffraction peaks in the XRD spectra reveal that all the investigated samples have typical hexagonal wurtzite structure. The pronounced diffraction peaks in the XRD pattern of $\text{Zn}_{0.98}\text{Mn}_{0.02}\text{O}$ nanopowder clearly shows the crystallite nature with peaks corresponding to the position 31.52° (100), 34.20° (002), 36.02° (101), 47.31° (102), 56.41° (110), 62.69° (103), 66.21° (200), 67.79° (112) and 68.96° (201). The diffraction data are in good agreement with the standard JCPDS file for ZnO (JCPDS 36-1451, $a = b = 3.249 \text{ \AA}$, $c = 5.206 \text{ \AA}$) with preferred orientation along (101) plane in all the samples. All the available reflections of the present XRD phases have been fitted with Gaussian distribution. It is evident from the XRD spectra that there are no extra peaks corresponding to Mn, Cu, oxides of Zn, Cu related secondary and impurity phases and indicate that Mn^{2+} ions would uniformly substitute into the Zn sites or interstitial sites in Zn–O lattice. Even though, there are no secondary phases detected by XRD analysis, the existence of secondary phases cannot be completely excluded due to limitation of this characterization technique [36].

Figure 2 shows the variation of diffraction intensity of $\text{Zn}_{0.98-x}\text{Mn}_{0.02}\text{Cu}_x\text{O}$ ($0 \leq x \leq 0.05$) nanopowders along (101) plane as a function of 2θ values from 35° to 37°. The insert of Fig. 2 shows the variation of peak position (2θ values) as a function of Cu concentrations. It is noticed from Fig. 2 that the peak position (2θ) of (101) plane has the

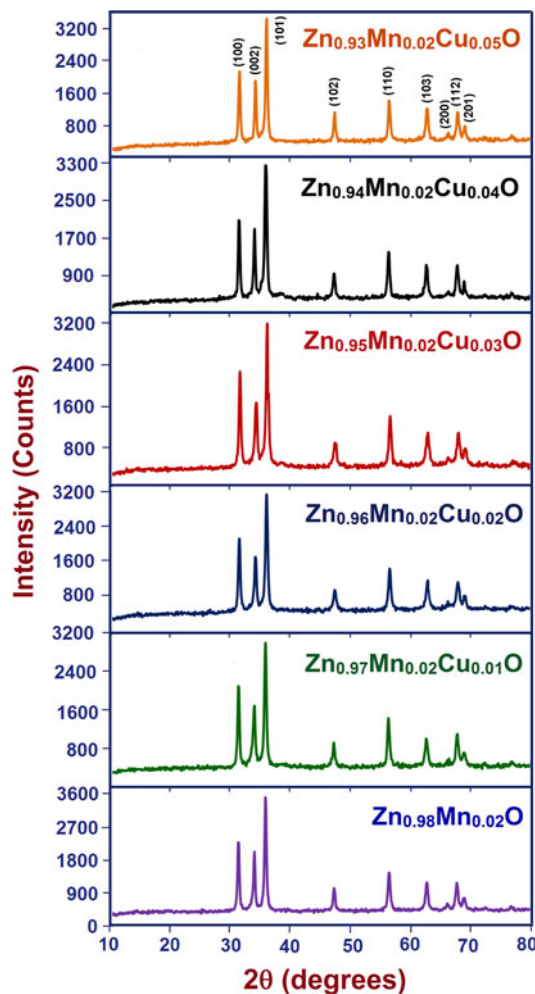


Fig. 1 Powder X-ray diffraction pattern of $\text{Zn}_{0.98-x}\text{Mn}_{0.02}\text{Cu}_x\text{O}$, $0 \leq x \leq 0.05$ nanopowders at room temperature

maximum value at $\text{Cu} = 2\%$ ($\text{Cu} = 0\text{--}2\%$), after that it is gradually decreased. At $\text{Cu} \leq 0.02$, the diffraction peaks shift towards the higher angles ($\Delta 2\theta = 35.99^\circ \sim 36.06^\circ = 0.07^\circ$) compared with the $\text{Zn}_{0.98}\text{Mn}_{0.02}\text{O}$. With the further increase of Cu concentrations ($x > 0.02$), the diffraction peaks shift towards the lower angles and is very small ($\Delta 2\theta = 36.06^\circ \sim 36.03^\circ = 0.03^\circ$).

The obvious decrease of (101) diffraction peak intensity with increasing Cu concentrations from 0 to 1 % as shown in Fig. 3 is due to the re-strain during the crystallization process compared with $\text{Zn}_{0.98}\text{Mn}_{0.02}\text{O}$. The peak intensity is almost constant between 1 and 3 % of Cu then it is gradually increased. But, Wei et al. [37] reported the steady increase of diffraction peak intensity by the addition of Cu. However, FWHM is increased up to 2 % and then gradually decreased. The observed change in diffraction peaks and the broadening are due to the increase of micro-strain [38]. But the line broadening may be due to the size, or micro-strain, or size and micro-strain [39]. The observed

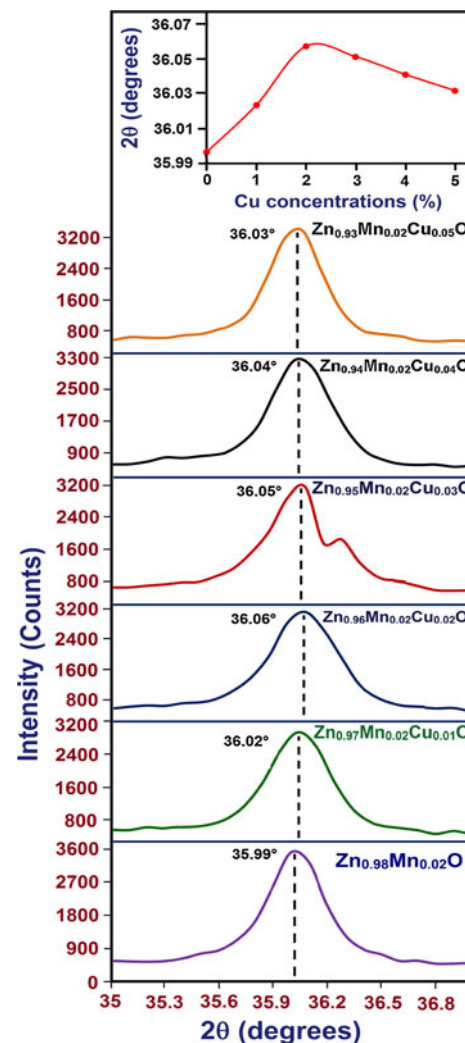


Fig. 2 The shift of X-ray diffraction peaks of $\text{Zn}_{0.98-x}\text{Mn}_{0.02}\text{Cu}_x\text{O}$, $0 \leq x \leq 0.05$ nanopowders along (101) plane. Inset shows the variation of 2θ as a function of Cu concentrations

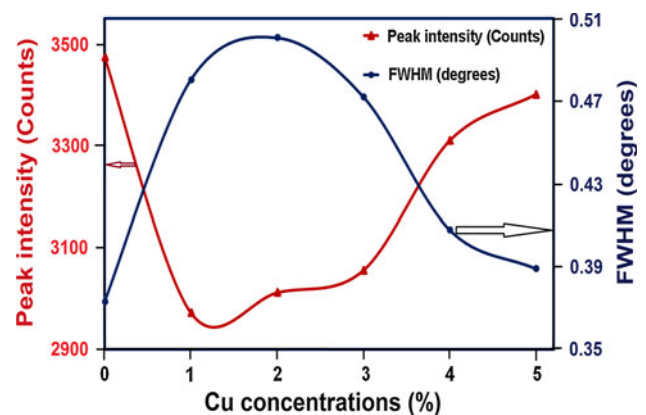


Fig. 3 The variation of peak intensity and full width at half maximum (FWHM, β) value of $\text{Zn}_{0.98-x}\text{Mn}_{0.02}\text{Cu}_x\text{O}$, $0 \leq x \leq 0.05$ nanopowders as a function of Cu concentrations

shift in the peak position and the broadening of the diffraction peaks illustrates the incorporation of Cu^{2+} ions into the Zn–O lattice and also indicates that the crystal lattice has no obvious change by Cu doping.

The average crystallite size of the samples is calculated after appropriate background correction from X-ray line broadening of the diffraction peaks along (101) plane using Debye–Scherrer's formula [40],

$$\text{Average crystallite size (D)} = \frac{0.9\lambda}{\beta \cos \theta} \quad (1)$$

where, λ is the wave length of X-ray used (1.5408 Å), β is the angular peak width at half maximum in radian along (101) plane and θ is the Bragg's diffraction angle. It is clearly noticed from Fig. 4 that the average crystallite size is gradually decreased from 22.38 to 16.69 nm by the addition of Cu from 0 to 2 % whereas it is increased from 16.69 to 21.47 nm by the addition of Cu from 2 to 5 %. It clearly shows the presence of nano-sized particles in the samples. The initial substitution of Cu^{2+} ions disturb the Zn–Mn–O lattice and decrease the nucleation and subsequent growth rate [41]. The reduction in crystallite size is due to the decrease of growth rate. The similar reduction of crystal size was observed at lower Cu concentrations in Cu doped ZnO system [42]. When $\text{Cu} > 0.02$, Cu^{2+} occupy the regular lattice site in Zn–O, the interference takes place between Mn and Cu metal ions and Zn–O lattice. Therefore, the crystallinity tends to enhance than the lower Cu concentrations.

Table 1 shows the variation of FWHM, average crystallite size (D) along (101) plane and micro-strain (ϵ) of $\text{Zn}_{0.98-x}\text{Mn}_{0.02}\text{Cu}_x\text{O}$ ($0 \leq x \leq 0.05$) nanopowders. The intrinsic stress is changed monotonically with increasing Cu concentrations due to change in the microstructure, size and shape of the particles. It is observed from Table 1 that micro-strain is gradually increased from Cu = 0 % (0.946×10^{-3}) to 2 % (1.269×10^{-3}) then gradually decreased up to Cu = 5 % (1.615×10^{-3}). It is evident that the increase of strain causes the decrease of crystallite

size, and the broadening and a small shift in XRD peaks where as the decrease of strain causes the increase of crystallite size and decrease the FWHM. The micro-strain (ϵ) can be calculated using the formula [43],

$$\text{Micro-strain } (\epsilon) = \frac{\beta \cos \theta}{4} \quad (2)$$

Table 2 shows the variation of peak position (2 θ), d-value, cell parameters 'a' and 'c', c/a ratio, bond length (l) and volume (V) of different $\text{Zn}_{0.98-x}\text{Mn}_{0.02}\text{Cu}_x\text{O}$ ($0 \leq x \leq 0.05$) nanopowders. Bond length and volume of the samples are calculated from cell parameters by using Eqs. (3) and (4) and are tabulated in Table 2. The Zn–O bond length has been calculated using the relationship [44],

$$\text{Bond length (l)} = \sqrt{\left(\frac{a^2}{3} + \left(\frac{1}{2} - u\right)c^2\right)} \quad (3)$$

where $u = \frac{d^2}{3c^2} + 0.25$, is the potential parameter of the hexagonal structure. The volume of unit cell of hexagonal system has been calculated from the equation [45],

$$\text{Volume (V)} = 0.866 \times a^2 \times c \quad (4)$$

At the lower Cu concentration ($\text{Cu} \leq 0.02$), the substitution of Cu^{2+} ions instead of Zn^{2+} ions at their lattice sites increases the lattice constant 'a' and 'c' and the interplanar distance 'd'. The similar trend of lattice constant was reported by Kulyk et al. [46] by Cu doping in ZnO which is consistent with our experimental result. Even though, the resultant compound maintains a wurtzite structure, the d-value and the lattice parameters 'a' and 'c' are slightly increases up to $x = 0.02$ and then decreases. The change in the lattice parameters could be well understood by the substitution of Cu^{2+} ions (ionic radius = 0.73 Å) which is larger than that of Zn^{2+} ions (ionic radius = 0.60 Å) [47] in their tetrahedral coordinates. Once Cu^{2+} ions replace Zn^{2+} , the bonding length of Cu–O will be higher in comparison with Mn–Zn–O. Thus, the lattice constant and hence the volume per unit cell will increase. At higher Cu concentrations ($\text{Cu} \geq 0.02$), the secondary phase of Cu emerged which indicates that the Cu ions and Mn ions

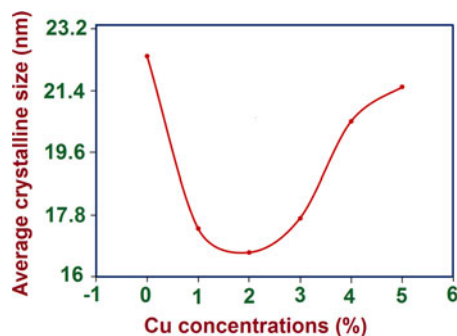


Fig. 4 The variation of average crystallite size (D) of $\text{Zn}_{0.98-x}\text{Mn}_{0.02}\text{Cu}_x\text{O}$, $0 \leq x \leq 0.05$ nanopowders as a function of Cu concentrations

Table 1 The variation of full width at half maximum (FWHM, β) value, average crystallite size (D) and micro-strain (ϵ) of different $\text{Zn}_{0.98-x}\text{Mn}_{0.02}\text{Cu}_x\text{O}$ ($0 \leq x \leq 0.05$) nanopowders

Samples	FWHM, β (°)	Average crystallite size, D (nm)	Micro-strain, ϵ (10^{-3})
$\text{Zn}_{0.98}\text{Mn}_{0.02}\text{O}$	0.3733	22.38	0.946
$\text{Zn}_{0.97}\text{Mn}_{0.02}\text{Cu}_{0.01}\text{O}$	0.4805	17.38	1.218
$\text{Zn}_{0.96}\text{Mn}_{0.02}\text{Cu}_{0.02}\text{O}$	0.5007	16.69	1.269
$\text{Zn}_{0.95}\text{Mn}_{0.02}\text{Cu}_{0.03}\text{O}$	0.4721	17.72	1.195
$\text{Zn}_{0.94}\text{Mn}_{0.02}\text{Cu}_{0.04}\text{O}$	0.4078	20.48	1.034
$\text{Zn}_{0.93}\text{Mn}_{0.02}\text{Cu}_{0.05}\text{O}$	0.3891	21.47	1.615

Table 2 The variation of peak position (2θ), d-value, cell parameters ‘a’ and ‘c’, c/a ratio, bond length (l) and volume (V) of different $\text{Zn}_{0.98-x}\text{Mn}_{0.02}\text{Cu}_x\text{O}$ ($0 \leq x \leq 0.05$) nanopowders

Samples	Peak position, 2θ ($^\circ$)	d-value (\AA)	Cell parameters (\AA)		c/a ratio	Bond length, l (\AA)	Volume, V (\AA^3)
			a = b	c			
$\text{Zn}_{0.98}\text{Mn}_{0.02}\text{O}$	35.99	2.4937	3.2750	5.2482	1.603	1.9933	48.7473
$\text{Zn}_{0.97}\text{Mn}_{0.02}\text{Cu}_{0.01}\text{O}$	36.02	2.4913	3.2761	5.2552	1.604	1.9946	48.8451
$\text{Zn}_{0.96}\text{Mn}_{0.02}\text{Cu}_{0.02}\text{O}$	36.06	2.4938	3.2786	5.2594	1.604	1.9995	48.9589
$\text{Zn}_{0.95}\text{Mn}_{0.02}\text{Cu}_{0.03}\text{O}$	36.05	2.4897	3.2684	5.2469	1.605	1.9898	48.539
$\text{Zn}_{0.94}\text{Mn}_{0.02}\text{Cu}_{0.04}\text{O}$	36.04	2.4905	3.2639	5.2455	1.607	1.9824	48.3925
$\text{Zn}_{0.93}\text{Mn}_{0.02}\text{Cu}_{0.05}\text{O}$	36.03	2.4911	3.2622	5.2394	1.606	1.9891	48.2859

would not only substitute the Zn place but also exist as interstitial ions or enter into vacancies. The presence of secondary phases/defects decreases the lattice constants, bond length and volume.

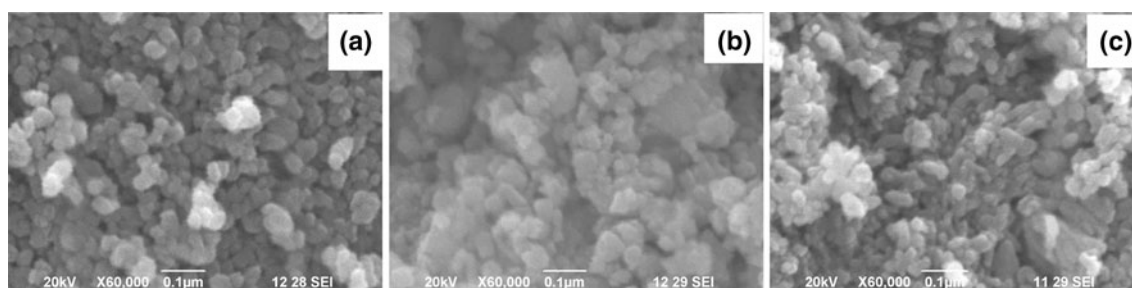
3.2 Scanning electron microscope (SEM)—microstructural studies

Scanning electron microscope (SEM) is one of the promising techniques to study the surface morphology of the samples and gives the important information regarding the growth mechanism, shape and size of the particles. The surface morphology of Mn-doped and Mn, Cu co-doped ZnO nanopowders are shown in Fig. 5a–c. SEM image of $\text{Zn}_{0.98}\text{Mn}_{0.02}\text{O}$ nanopowder (Fig. 5a) shows that the nanoparticles are homogeneous, uniformly distributed over the surface and good connectivity between the particles containing dominated spheroid-like structure with particle size around 10–30 nm. The further increase of Cu decreases the particle size. Figure 5b shows the surface morphology of $\text{Zn}_{0.96}\text{Mn}_{0.02}\text{Cu}_{0.02}\text{O}$ nanopowder which has lower particle size than $\text{Zn}_{0.98}\text{Mn}_{0.02}\text{O}$ nanopowders. The SEM (Fig. 5b) shows the uneven surface morphology with very fine loosely agglomerated and deformed spherical nanoparticles in a spongy porous network having the particle size between 7 and 20 nm.

However, the crystal quality of the system is remarkably improved by the further increase of Cu in Zn–Mn–O lattice. Figure 5c shows microstructure of $\text{Zn}_{0.93}\text{Mn}_{0.02}\text{Cu}_{0.05}\text{O}$, which has higher particle size than $\text{Zn}_{0.96}\text{Mn}_{0.02}\text{Cu}_{0.02}\text{O}$. It contains mixer of spheroid-like and rod-like particles where spheroid-like particles are dominant with particle size around 10–28 nm. It is evident that the decrease of strain causes the reduction of particle size (Table 1). A good correlation is found to exist between XRD and SEM studies.

3.3 Energy dispersive X-ray (EDX) spectra

Chemical purity and stoichiometry of the samples are tested by EDX spectra. The typical EDX spectra of $\text{Zn}_{0.98-x}\text{Mn}_{0.02}\text{Cu}_x\text{O}$ ($x = 0, 0.02$ and 0.05) nanopowders are shown in Fig. 6. The quantitative atomic and weight percentage of the compositional elements such as Zn, Mn, Cu and O present in $\text{Zn}_{0.98-x}\text{Mn}_{0.02}\text{Cu}_x\text{O}$ ($x = 0, 0.02$ and 0.05) nanopowders are given in Table 3. The EDX spectra confirm the presence of appropriate amount of Mn and Cu in ZnO and purity of system. It is observed from Fig. 6 that the weight percentage of $\text{Cu}/(\text{Zn} + \text{Mn})$ ratio is derived to be 1.9 and 5.4 %, whereas atomic percentage is derived to be 2.2 and 4.8 % for $\text{Zn}_{0.96}\text{Mn}_{0.02}\text{Cu}_{0.02}\text{O}$, $\text{Zn}_{0.93}\text{Mn}_{0.02}\text{Cu}_{0.05}\text{O}$, respectively. The calculated weight and atomic percentage are nearly equal to their nominal stoichiometry within the experimental error.

**Fig. 5** Scanning electron microscope (SEM) images of **a** $\text{Zn}_{0.98}\text{Mn}_{0.02}\text{O}$, **b** $\text{Zn}_{0.96}\text{Mn}_{0.02}\text{Cu}_{0.02}\text{O}$ and **c** $\text{Zn}_{0.93}\text{Mn}_{0.02}\text{Cu}_{0.05}\text{O}$ nanopowders at room temperature

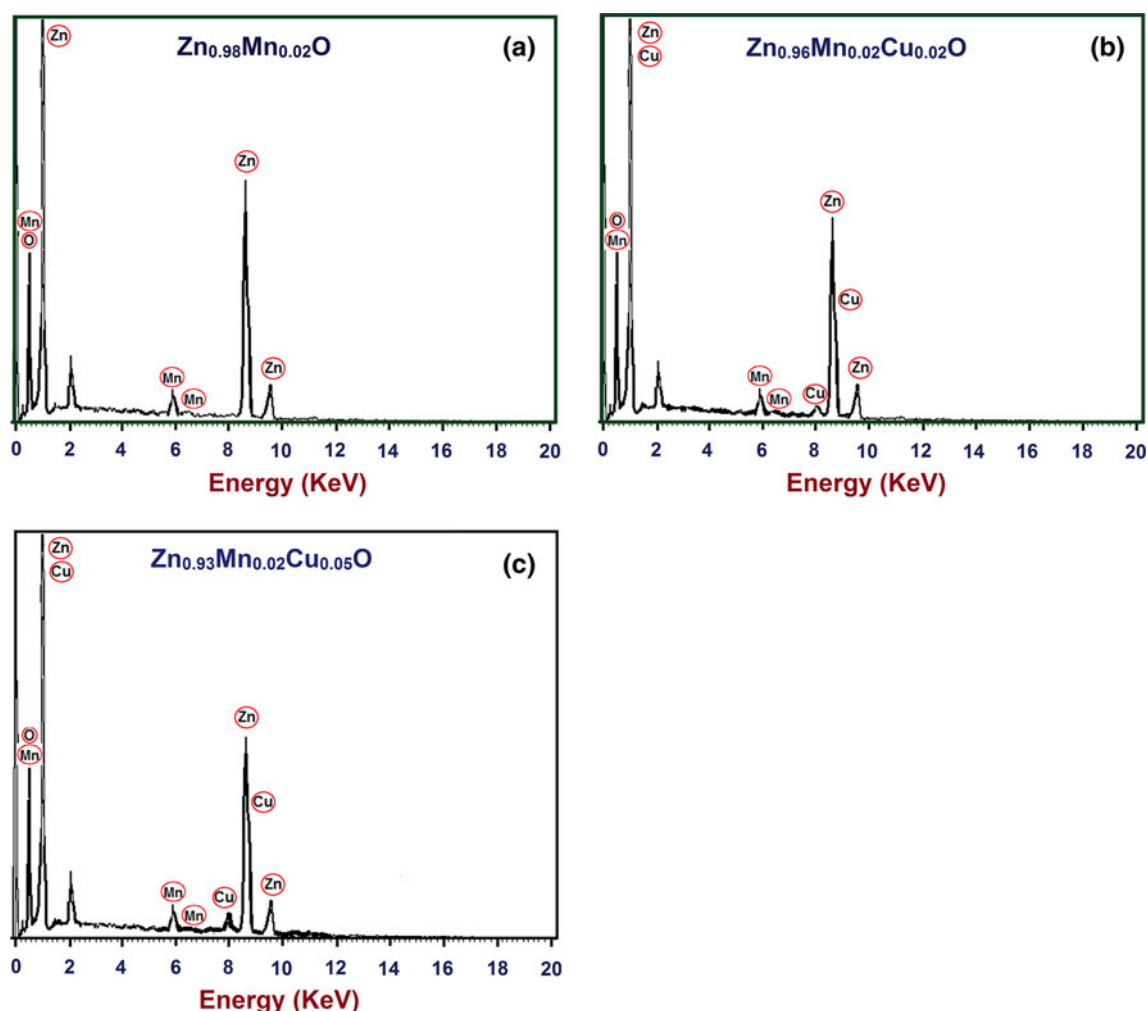


Fig. 6 Energy dispersive X-ray (EDX) spectra of **a** $\text{Zn}_{0.98}\text{Mn}_{0.02}\text{O}$, **b** $\text{Zn}_{0.96}\text{Mn}_{0.02}\text{Cu}_{0.02}\text{O}$ and **c** $\text{Zn}_{0.93}\text{Mn}_{0.02}\text{Cu}_{0.05}\text{O}$ nanopowders at room temperature

Table 3 The quantitative analysis of the compositional elements present in the different $\text{Zn}_{0.98-x}\text{Mn}_{0.02}\text{Cu}_x\text{O}$ ($0 \leq x \leq 0.05$) nanopowders using EDX analysis

Samples	Percentage of the elements (%)									
	Weight (%)				Cu/(Zn + Mn) ratio	Atomic (%)				Cu/(Zn + Mn) ratio
	Zn	O	Mn	Cu		Zn	O	Mn	Cu	
$\text{Zn}_{0.98}\text{Mn}_{0.02}\text{O}$	66.34	32.31	1.33	–	–	51.94	46.85	1.21	–	–
$\text{Zn}_{0.96}\text{Mn}_{0.02}\text{Cu}_{0.02}\text{O}$	65.46	31.78	1.47	1.29	0.019	51.32	46.34	1.18	1.16	0.022
$\text{Zn}_{0.93}\text{Mn}_{0.02}\text{Cu}_{0.05}\text{O}$	64.82	30.11	1.46	3.61	0.054	50.31	46.03	1.17	2.49	0.048

3.4 Optical properties

UV–visible absorption spectroscopy is a powerful technique to explore the optical properties of semiconducting nanoparticles. The UV–visible optical absorption spectra of Cu, Mn co-doped ZnO ($\text{Zn}_{0.98-x}\text{Mn}_{0.02}\text{Cu}_x\text{O}$, $0 \leq x \leq 0.05$) nanopowders are recorded at room temperature using UV–visible spectrometer (Model: Lambda 35, Make: Perkin Elmer) from

310 to 1,100 nm as shown in Fig. 7a, b shows the enlarged picture of absorption changes between 310 and 408 nm.

The absorption of $\text{Zn}_{0.98-x}\text{Mn}_{0.02}\text{Cu}_x\text{O}$ nanopowder is increased when the Cu concentration increases from 0 to 0.04 and the further increase of Cu reduces the absorption where $\text{Zn}_{0.94}\text{Mn}_{0.02}\text{Cu}_{0.04}\text{O}$ sample has a maximum value. It is observed from Fig. 7 that all the samples shows a broad absorption peak around 500–406 nm except $\text{Zn}_{0.98}\text{Mn}_{0.02}\text{O}$

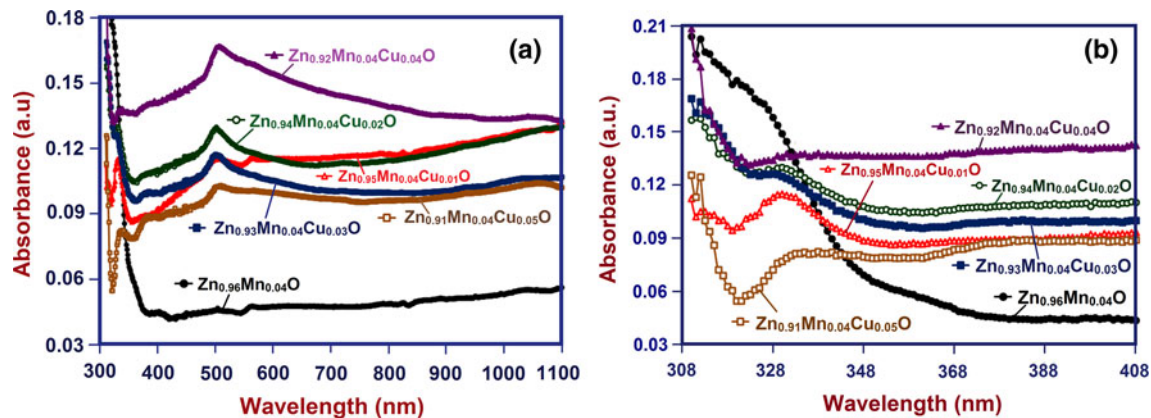


Fig. 7 UV-visible absorption spectra of $\text{Zn}_{0.98-x}\text{Mn}_{0.02}\text{Cu}_x\text{O}$, $0 \leq x \leq 0.05$ nanopowders as a function of wavelength from **a** 300–1,100 nm and **b** 300–408 nm

which has no peak. The intensity and FWHM of these peaks increases up to $\text{Cu} = 0.04$ then decreases. The absorption peak appearing at 499 nm for $\text{Zn}_{0.97}\text{Mn}_{0.02}\text{Cu}_{0.01}\text{O}$ nanopowder is slightly shifted towards the higher wavelengths (red shift) by Cu doping; $\text{Zn}_{0.96}\text{Mn}_{0.02}\text{Cu}_{0.02}\text{O}$ sample has 502 nm; $\text{Zn}_{0.95}\text{Mn}_{0.02}\text{Cu}_{0.03}\text{O}$ sample has 500 nm; $\text{Zn}_{0.94}\text{Mn}_{0.02}\text{Cu}_{0.04}\text{O}$ sample has 504 nm; $\text{Zn}_{0.93}\text{Mn}_{0.02}\text{Cu}_{0.05}\text{O}$ sample has 506 nm. The noticed change in absorption can be attributed to the photo-excitation of electrons from valence band to conduction band. The similar red shift of absorption band was noticed in the literature [39] by Cu-doping.

The typical room temperature transmittance spectra of $\text{Zn}_{0.96-x}\text{Mn}_{0.04}\text{Cu}_x\text{O}$ nanopowders are shown in Fig. 8. The transmission spectra of $\text{Zn}_{0.96-x}\text{Mn}_{0.04}\text{Cu}_x\text{O}$ nanopowders show just opposite trend of the optical absorption spectra. It is clear from Fig. 8 that all the samples exhibit a high transmittance. A sharp decrease in transmittance around 499–506 nm is due to the band edge absorption [48]. This strong absorption explores that the incoming photons have sufficient energy to excite electrons from the valence band to the conduction band. The optical band gap is calculated using the Tauc relation [49],

$$\alpha h\nu = A * (h\nu - E_g)^n \quad (5)$$

where, A^* is a constant, $h\nu$ is the incident photon energy, E_g is the energy band gap of the material and the exponent $n = 1/2$ for allowed direct band gap.

The energy band gap (E_g) of Mn, Cu co-doped ZnO ($\text{Zn}_{0.98-x}\text{Mn}_{0.02}\text{Cu}_x\text{O}$, $0 \leq x \leq 0.05$) nanopowders can be obtained by plotting $(\alpha h\nu)^2$ versus $h\nu$ and extrapolating the linear portion of the absorption edge to find the intercept with energy axis as shown in Fig. 9a. The variation of E_g as a function of Cu concentrations is shown in Fig. 9b. The band gap is initially decreases (red shift) from $\text{Cu} = 0\%$ (3.6 eV) to 3 % (3.33 eV) ($E_g \approx 0.27$ eV) at lower Cu concentrations meanwhile it is increases (blue shift) from

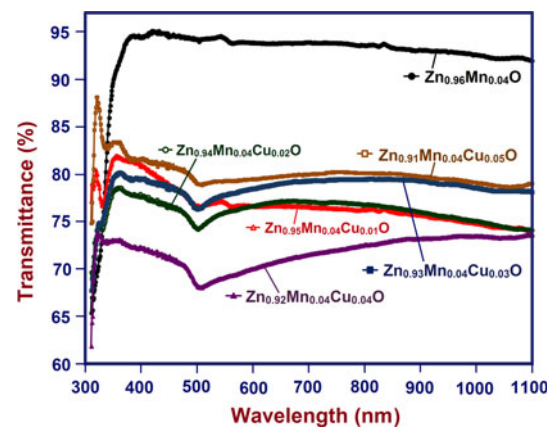


Fig. 8 Transmittance spectra of $\text{Zn}_{0.98-x}\text{Mn}_{0.02}\text{Cu}_x\text{O}$, $0 \leq x \leq 0.05$ nanopowders as a function of wavelength

$\text{Cu} = 3\%$ (3.33 eV) to 5 % (3.86 eV) ($E_g \approx 0.56$ eV) at higher Cu concentrations. The observed red shift of E_g at lower concentrations ($\text{Cu} = 0 \rightarrow 3\%$) is due to the initial substitution of Cu in the Mn–Zn–O lattice. The red shift in the band gap is theoretically explained by Bylsma et al. [50] using the s–d and p–d exchange interactions using the second-order perturbation theory. During the substitution of Cu^{2+} ions instead of Zn^{2+} ions, the carrier concentration is increased and consequently the band gap is reduced which could be due to the Moss–Burstein effect [51]. The similar red shift was observed by Diouri et al. and explained by the p–d spin-exchange interactions between the band electrons and the localized d electrons of Cu^{2+} ion [52], thereby shrinking the band gap. The observed blue shift at higher Cu concentrations is explained in terms of the distortion of host lattice and generation of defects, but these factors would not play a main role in the determination of band gap energy [53]. The variation of crystallite size and energy gap of $\text{Zn}_{0.98-x}\text{Mn}_{0.02}\text{Cu}_x\text{O}$ nanopowders

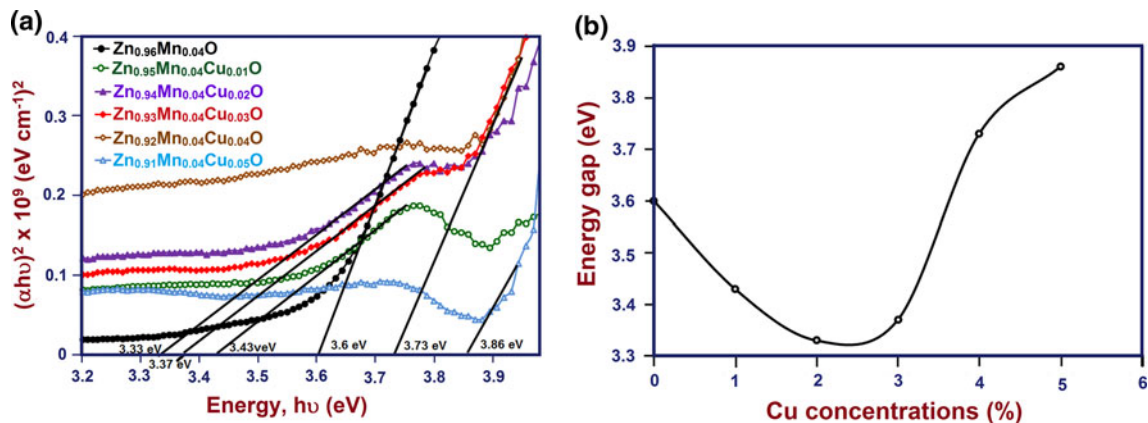


Fig. 9 **a** The $(\alpha h\nu)^2$ versus $h\nu$ curves for the optical band gap determination of $\text{Zn}_{0.98-x}\text{Mn}_{0.02}\text{Cu}_x\text{O}$, $0 \leq x \leq 0.05$ nanopowders, **b** the variation of energy gap (E_g) as a function of Cu concentrations

by Cu-doping made the samples as a promising candidate for the preparation of opto-electronic devices.

4 Conclusions

$\text{Zn}_{0.98-x}\text{Mn}_{0.02}\text{Cu}_x\text{O}$, $0 \leq x \leq 0.05$ nanopowders have been successfully synthesized by sol–gel method. The XRD and SEM measurements revealed the different microstructure without changing a hexagonal wurtzite structure. The EDX spectra confirmed the presence of Cu in Mn–Zn–O system and the atomic and weight percentage were nearly equal to their nominal stoichiometry within the experimental error. The calculated average crystallite size decreased from 22.4 to 16.7 nm for $\text{Cu} = 0\text{--}0.02$ then gradually increased to 21.5 nm for $\text{Cu} = 0.05$ which were confirmed by SEM. The change in lattice parameters, shift in X-ray diffraction peaks and the change in energy gap revealed the substitution of Cu^{2+} ions into Zn–Mn–O lattice. The observed red shift of optical energy gap ($E_g \approx 0.27$ eV) at lower concentrations ($\text{Cu} \leq 2\%$) is explained by increasing charge carriers and Moss–Burstein effect meanwhile blue shift ($E_g \approx 0.56$ eV) at higher Cu concentrations ($\text{Cu} > 2\%$) is explained in terms of the distortion of host lattice and generation of defects. The variation of crystallite size and energy gap of $\text{Zn}_{0.98-x}\text{Mn}_{0.02}\text{Cu}_x\text{O}$ nanopowders by Cu-doping made the samples as a promising candidate for the preparation of opto-electronic devices.

Acknowledgments The authors are thankful to the University Grant Commission, Hyderabad, for financial support under the project (File No.: MRP- 3610/11(MRP/UGC-SERO)).

References

1. V.V. Malyshev, A.V. Pislyakov, *Sens. Actuators B Chem.* **123**, 71 (2007)

2. A. Dodd, A. McKinley, M. Saunders, T. Tsuzuki, *Nanotechnology* **17**, 692 (2006)
3. C. Jagadish, S. Pearton (eds.), *Zinc oxide bulk, thin films and nanostructures, in Processing, Properties, and Applications*, 1st edn. (Elsevier, Oxford, 2006)
4. H. Ohno, *Science* **281**, 951 (1998)
5. J. Goldberger, R.R. He, Y.F. Zhang, S.W. Lee, H.Q. Yan, H.J. Choi, P. Yang, *Nature* **422**, 599 (2003)
6. O.D. Jayakumar, I.K. Gopalakrishnan, *Appl. Phys. Lett.* **89**, 202507 (2006)
7. I. Malajovich, J.J. Berry, N. Samarth, D.D. Awschalom, *Nature* **411**, 770 (2001)
8. Q. Yan, R. He, J. Pham, P.D. Yang, *Adv. Mater.* **15**, 402 (2003)
9. S. Deka, P.A. Joy, *Appl. Phys. Lett.* **89**, 032508 (2006)
10. R. Konekamp, R.C. Word, C. Schlegel, *Appl. Phys. Lett.* **85**, 6004 (2004)
11. J.J. Chen, F. Zeng, D.M. Li, J.B. Niu, F. Pan, *Thin Solid Films* **484**, 257 (2005)
12. A. Fert, *Thin Solid Films* **517**, 2 (2008)
13. Y.M. Tao, S.Y. Ma, H.X. Chen, J.X. Meng, L.L. Hou, Y.F. Jia, X.R. Shang, *Vacuum* **85**, 744 (2011)
14. Z. Zhang, J.B. Yi, J. Ding, L.M. Wong, H.L. Seng, S.J. Wang, J.G. Tao, G.P. Li, G.Z. Xing, T.C. Sum, C.H.A. Huan, T. Wu, *J. Phys. Chem.* **C112**, 9579 (2008)
15. C.F. Jin, X. Yuan, W.W. Ge, J.M. Hong, X.Q. Xin, *Nanotechnology* **14**, 667 (2003)
16. H. Udono, Y. Sumi, S. Yamada, I. Kikuma, *J. Cryst. Growth* **310**, 1827 (2008)
17. T. Tsuzuki, P.G. McCormick, *Scr. Mater.* **44**, 1731 (2001)
18. Y. Dai, Y. Zhang, Q.K. Li, C.W. Nan, *Chem. Phys. Lett.* **358**, 83 (2002)
19. C.L. Zhang, W.N. Zhou, Y. Hang, Z. Lu, H.D. Hou, Y.B. Zuo, S.J. Qin, F.H. Lu, S.L. Gu, *J. Cryst. Growth* **310**, 1819 (2008)
20. S.E. Ahn, J.S. Lee, H. Kim, S. Kim, B.H. Kang, K.H. Kim, G.T. Kim, *Appl. Phys. Lett.* **84**, 5022 (2004)
21. I.R. Collins, S.E. Taylor, *J. Mater. Chem.* **2**, 1277 (1992)
22. D. Jezequel, J. Guenet, N. Jouini, F. Fievet, *J. Mater. Res.* **10**, 77 (1995)
23. L. Poul, S. Ammar, N. Jouini, F. Fievet, F. Villain, *Solid State Sci.* **3**, 31 (2001)
24. L. Poul, S. Ammar, N. Jouini, F. Fievet, F. Villain, *J. Sol–Gel Sci. Technol.* **26**, 261 (2003)
25. S. Lee, S. Jeong, D. Kim, S. Hwang, M. Jeon, J. Moon, *Super Lattices Microstruct.* **43**, 330 (2008)
26. M. Arshad, A. Azam, A.S. Ahmed, S. Mollah, A.H. Naqvi, *J. Alloys Compd.* **509**, 8378 (2011)

27. S. Muthukumaran, R. Gopalakrishnan, J. Mater. Sci.: Mater. Electron. **23**, 1393 (2012)
28. X.M. Teng, H.T. Fan, S.S. Pan, C. Ye, G.H. Lia, J. Appl. Phys. **100**, 053507 (2006)
29. B.N. Dole, V.D. Mote, V.R. Huse, Y. Purushotham, M.K. Lande, K.M. Jadhav, S.S. Shah, Curr. Appl. Phys. **11**, 762 (2011)
30. J. Yang, L. Fei, H. Liu, Y. Liu, M. Gao, Y. Zhang, L. Yang, J. Alloys Compd. **509**, 3672 (2010)
31. H. Liu, J. Yang, Z. Hua, Y. Zhang, L. Yang, L. Xiao, Z. Xie, Appl. Surf. Sci. **256**, 4162 (2010)
32. H. Xu, Q. Zhao, H. Yang, Y. Chen, J. Nanopart. Res. **11**, 615 (2009)
33. S.J. Han, J.W. Song, C.H. Yang, S.H. Park, J.H. Parket, J.H. Jeong, Appl. Phys. Lett. **81**, 4212 (2002)
34. J. Shim, T. Hwang, J. Park, S.J. Han, Y. Jeong, Appl. Phys. Lett. **86**, 082503 (2005)
35. H. Liu, J. Yang, Z. Hua, Y. Liu, L. Yang, Y. Zhang, J. Cao, Mater. Chem. Phys. **125**, 656 (2011)
36. A. Askarinejad, A. Morsali, Ultrason. Sonochem. **16**, 124 (2009)
37. Y. Wei, D. Hou, S. Qiao, C. Zhen, G. Tang, Physica B **404**, 2486 (2009)
38. J.H. Zheng, J.L. Song, Q. Jiang, J.S. Lian, Appl. Surf. Sci. **258**, 6735 (2012)
39. A. Jagannatha Reddy, M.K. Kokila, H. Nagabhushan, R.P.S. Chakradhar, C. Shivakumar, J.L. Rao, B.M. Nagabhushan, J. Alloys Compd. **509**, 5349 (2011)
40. S. Muthukumaran, R. Gopalakrishnan, Physica B **407**, 3448 (2012)
41. P.K. Sharma, R.K. Dutta, A.C. Pandey, J. Magn. Magn. Mater. **321**, 4001 (2009)
42. S. Muthukumaran, R. Gopalakrishnan, Optical Mater. **34**, 1946 (2012)
43. P.P. Hankare, P.A. Chate, D.J. Sathe, P.A. Chavan, V.M. Bhuse, J. Mater. Sci.: Mater. Electron. **20**, 374 (2009)
44. B.D. Cullity, *Elements of X-ray Diffractions* (Addison-Wesley, Reading, 1978)
45. G. Srinivasan, R.T.R. Kumar, J. Kumar, J. Sol–Gel Sci. Technol. **43**, 171 (2007)
46. B. Kulyk, B. Sahraoui, V. Figà, B. Turko, V. Rudyk, V. Kapustianyk, J. Alloys Compd. **481**, 819 (2009)
47. Y. Liu, J.H. Yang, Q.F. Guan, L.L. Yang, Y.J. Zhang, Y.X.W. Feng, J. Cao, X.Y. Liu, Y.T. Yang, M.B. Wei, J. Alloys Compd. **486**, 835 (2008)
48. R. Gopalakrishnan, S. Muthukumaran, J. Mater. Sci.: Mater. Electron. **24**, 1069 (2013)
49. S. Suwanboon, P. Amornpitoksuk, A. Haidoux, J.C. Tedenac, J. Alloys Compd. **462**, 335 (2008)
50. R.B. Bylsma, W.M. Becker, J. Kossut, U. Debska, D. Yoder-Short, Phys. Rev. B **33**, 8207 (1986)
51. B. Joseph, P.K. Manoj, V.K. Vaidyah, Ceramics Int. **32**, 487 (2006)
52. J. Diouri, J.P. Lascaray, M.E. Amrani, Phys. Rev. B **31**, 7995 (1985)
53. A.P. Palomino, O.P. Perez, R. Singhal, M. Tomar, J. Hwang, P.M. Voyles, J. Appl. Phys. **103**, 07D121 (2008)